Publication Year	2015
Acceptance in OA@INAF	2020-07-09T10:31:33Z
Title	Temporal Evolution of Multiple Evaporating Ribbon Sources in a Solar Flare
Authors	Graham, D. R.; CAUZZI, Gianna
DOI	10.1088/2041-8205/807/2/L22
Handle	http://hdl.handle.net/20.500.12386/26401
Journal	THE ASTROPHYSICAL JOURNAL LETTERS
Number	807

The Astrophysical Journal Letters, 807:L22 (5pp), 2015 July 10 doi:10.1088/2041-8205/807/2/L22

© 2015. The American Astronomical Society. All rights reserved.

TEMPORAL EVOLUTION OF MULTIPLE EVAPORATING RIBBON SOURCES IN A SOLAR FLARE

D. R. Graham and G. Cauzzi
INAF-Osservatorio Astrofisico di Arcetri, I-50125 Firenze, Italy; dgraham@arcetri.astro.it

Received 2015 May 1; accepted 2015 June 10; published 2015 July 6

ABSTRACT

We present new results from the *Interface Region Imaging Spectrograph* (*IRIS*) showing the dynamic evolution of chromospheric evaporation and condensation in a flare ribbon, with the highest temporal and spatial resolution to date. *IRIS* observed the entire impulsive phase of the X-class flare SOL2014-09-10T17:45 using a 9.4 s cadence "sit-and-stare" mode. As the ribbon brightened successively at new positions along the slit, a unique impulsive phase evolution was observed for many tens of individual pixels in both coronal and chromospheric lines. Each activation of a new footpoint displays the same initial coronal upflows of up to ~300 km s^{-1} and chromospheric downflows up to 40 km s^{-1}. Although the coronal flows can be delayed by over 1 minute with respect to those in the chromosphere, the temporal evolution of flows is strikingly similar between all pixels and consistent with predictions from hydrodynamic flare models. Given the large sample of independent footpoints, we conclude that each flaring pixel can be considered a prototypical, "elementary" flare kernel.

Key words: Sun: activity – Sun: chromosphere – Sun: flares – Sun: transition region – Sun: UV radiation

1. INTRODUCTION

Spectral signatures of chromospheric evaporation during a flare's impulsive phase have long been observed as strongly blueshifted components of very hot, "coronal" lines (see, e.g., the review by Milligan 2015). However, the common occurrence of a dominant stationary component, together with the blueshifted one, remained in contrast to the predictions of theory for single flaring loops (e.g., Li et al. 1989; Mariska et al. 1989). A likely scenario to resolve this discrepancy invokes highly filamentary structures in which many sub-resolution magnetic loops are activated in succession. Emission would be detectable only when a number of these loops emit together, and the evaporated plasma in many of them has come to rest (e.g., Hori et al. 1997; Doschek & Warren 2005). In the 1990s and 2000s, spatially resolved observations from EUV spectrometers such as *SOHO*/CDS (Harrison et al. 1995) and *Hinode*/EIS (Culhane et al. 2007), started providing support to this idea. A few authors reported the occurrence of fully blueshifted high-temperature lines within flaring footpoints, corresponding to upflows of ~150–250 km s^{-1} (e.g., Brosius 2013). Yet, such occurrences remained sporadic in the literature.

The low-temperature counterpart of evaporation, required to conserve momentum (chromospheric condensation; Fisher 1987), has also been observed numerous times by the CDS and EIS spectrometers, although the temperature at which downflows are observed varies greatly depending on the flare observed (Milligan et al. 2006; Milligan & Dennis 2009; Graham et al. 2011). To date, the most comprehensive studies of the spatio-temporal evolution of chromospheric condensation have been performed using ground-based observations of optically thick chromospheric lines such as Hα or Ca II (e.g., Canfield et al. 1990). For example, the high-resolution observations of Falchi et al. (1997) proved that chromospheric condensation occurs only in very small areas ($<1''$) at the leading edge of a flaring ribbon, in agreement with the filamentary scenario outlined above.

The *Interface Region Imaging Spectrograph* (*IRIS*; De Pontieu et al. 2014) is rapidly providing new insights into this topic. With simultaneous imaging and spectroscopy in the near-UV, *IRIS* covers a variety of continua and emission lines formed over the chromosphere (~10^4 K), transition region, and corona. Equally important, its high spatial, temporal, and spectral resolution will provide for more stringent testing for models of flare heating and chromospheric dynamics. Indeed, several *IRIS* papers already have documented fully blueshifted profiles of the coronal Fe XXI line in flares (Sadykov et al. 2014; Tian et al. 2014, 2015; Polito et al. 2015; Young et al. 2015).

In this Letter, we use high-cadence *IRIS* data to provide a comprehensive picture of chromospheric evaporation and condensation, tracking the entire impulsive phase evolution of tens of unique, sequentially activated, ribbon sources in an X-class flare.

2. DATA ANALYSIS

The GOES X1.6 class flare SOL2014-09-10T17:45 developed in AR NOAA 12158 near disk center (N15E02), with a complex two-ribbon structure that encompassed the main, leading polarity sunspot, and a group of several smaller spots of following polarity (see Figures 1 and 4 and the studies of Li & Zhang 2015 and Tian et al. 2015). During the impulsive phase, a rapid increase of the 20–100 keV hard X-ray flux was observed by Fermi (Meegan et al. 2009) starting from ~17:22 UT, peaking around 17:36 UT. We focus on plasma dynamics during this early impulsive phase.

A flare watch program was run by *IRIS* on NOAA 12158 from 11:28 UT to 17:58 UT, using sit-and-stare mode and the standard *IRIS* flare line list (OBSID 3860259453). The exposure time throughout was 8 s for the FUV channel, while in the NUV it was dropped from 8 to 2.4 s at 17:27 UT; the cadence was kept a constant 9.4 s for both channels, one of the highest ever for such a study.

The left panel of Figure 1 represents the full *IRIS* 1400 Å slit-jaw image at 17:22 UT, showing the early development of the ribbons. The vertical black line indicates the spectrograph slit. The four smaller panels on the right show the central region for different times during the impulsive phase. Comparing with the horizontal dashed line at $y = 122''$ demonstrates how the ribbon

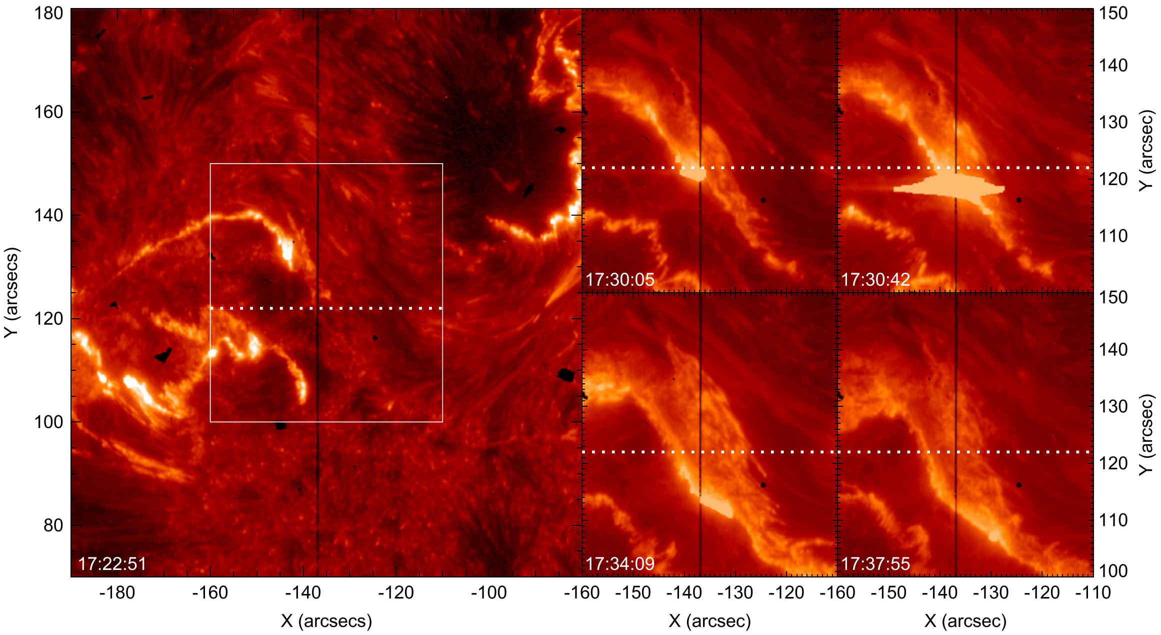

Figure 1. *IRIS* 1400 Å slit-jaw images (SJI) showing the evolution of the flaring region. The full field of view is seen in the larger left panel, and the four smaller panels display the ribbon evolution in the central area (white box) during the impulsive phase. Note that the 1400 Å SJI images saturate at times, but the spectra analyzed remain below this level.

developed southward along a portion of the slit and the successive brightening of individual footpoint kernels over previously undisturbed regions.

2.1. *Fe xxi Analysis*

A single high-temperature line, Fe xxi 1354.1 Å formed at ~10 MK, is found in the *IRIS* spectral windows (see Young et al. 2015). We prepared the data using the *Solarsoft IRIS*_GETWINDATA procedure, which returns the spectrum in photon counts with uncertainties. A spatial binning of ±1 pixel along the slit direction was used to improve the signal to noise ratio; the Fe xxi data shown hence have a spatial scale of $0\overset{\prime\prime}{.}33$ (slit width) × $0\overset{\prime\prime}{.}5$.

The UV Fe xxi emissivity is generally low, yet the 1354.1 Å line has been clearly observed during flares in earlier observations (Mason et al. 1986; Cheng 1990). In our X-class event, we detect emission during the entire flare evolution, but the concomitant presence of flare-enhanced lines from cooler ions, including Si ii, Fe ii, and C i, requires special care in order to extract the Fe xxi signal. We make Gaussian fits to the strong lines present in the 1352.4–1355.9 Å spectral window (labeled in Figure 2), allowing for the presence of a second, redshifted component of the cooler lines when necessary. The fit was further constrained by locking the centroids and widths of the Si ii and Fe ii lines to the same species present in the adjacent 1347.8–1350.9 Å spectral window.

In Figure 2, the fit to the Fe xxi line is shown for slit position $y = 122''$ and for the four time steps of the right panels of Figure 1. In the earliest frame, the Fe xxi line is shifted almost to the blue edge of the spectral window, with an upflow velocity of 280 km s^{-1}; its deceleration is easily tracked in time moving toward the rest wavelength at 1354.1 Å.

A similar fit was performed over all of the flaring slit pixels. In most of them, the earliest instance of the line is extremely broad and of comparable intensity to the background chromospheric lines; to avoid misidentification, we have tracked the Fe xxi enhancement back in time by examining the series of spectra by eye, determining when the flow speed stops increasing or the line is otherwise undetectable. Fits prior to this cutoff are not included in the analysis. Nowhere do we find evidence for a separate "stationary component" of the Fe xxi line: the chromospheric lines are well identified and there is no significant residual between the fit and data to suggest that one exists.

2.2. *Mg ii Analysis*

The Mg ii resonance h&k lines, as well as their subordinate triplet, are among the best chromospheric diagnostics within the *IRIS* spectral range, even for flaring conditions (Leenaarts et al. 2013; Pereira et al. 2015). As the h&k lines saturated in several of the brightest flaring pixels within our flare, we identified the subordinate 2791.6 Å as the best candidate for studying chromospheric condensation: the line is several Å removed from the Mg ii k, hence less influenced by its variations during flares than the self-blended component at 2798.7 Å.

The data were prepared using the same method as Fe xxi; however, given the stronger signal, we maintain the original pixel scale of $0\overset{\prime\prime}{.}33 \times 0\overset{\prime\prime}{.}166$. The rest wavelength was determined by averaging the line core position in a non-flaring region over the multi-hour observation and accounting for the spacecraft orbit variation; we estimate the velocity zero point to ±0.7 km s^{-1}.

As proven by ground-based observations, useful indications about the amplitude and evolution of the chromospheric condensation can be obtained from optically thick lines by measuring their bisector, i.e., the locus of mid-points measured at different intensity levels within the line (see Ding et al. 1995). In Figure 2 (right panels), we show the Mg ii 2791.6 Å line profiles as observed in the same pixel and times as the corresponding Fe xxi panels. The shape and characteristics of the Mg ii lines are consistent with older results

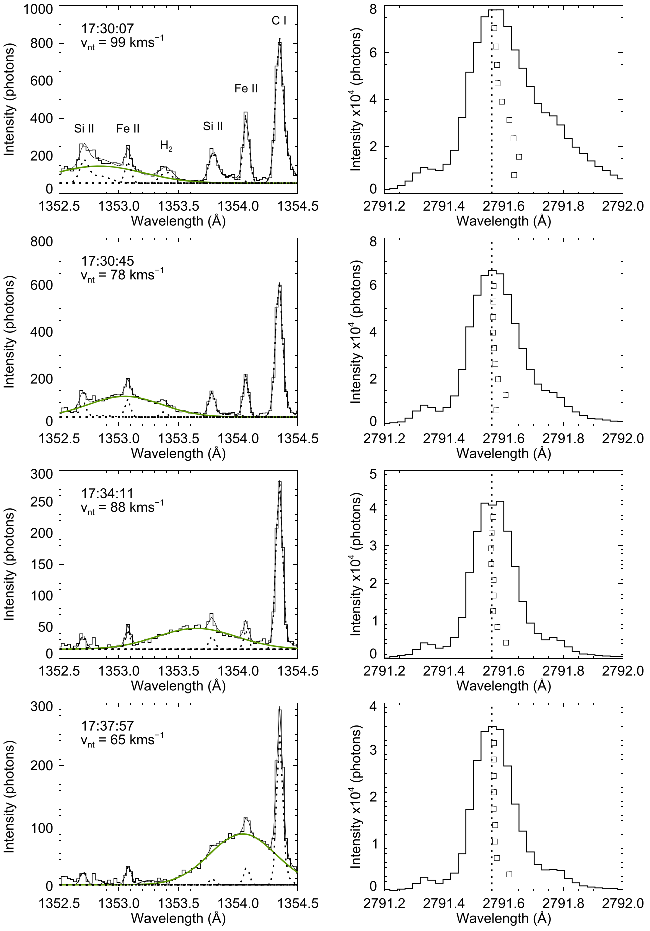

Figure 2. Left panels: fits of the Fe xxi 1354.1 Å line (green) for slit position $y = 122''$. The observed spectrum is shown by the stepped black line, with the total fit in black on top; cooler components are shown by a dotted line. The non-thermal FWHM, $v_{\rm nt}$, is also shown. Right panels: Mg ii subordinate line with bisector positions at 10% intensity increments marked by black squares, and the rest wavelength (2791.56 Å) by the vertical dashed line.

(Canfield et al. 1990; Ding et al. 1995): almost all the flaring pixels initially display a red asymmetry of the line, which disappears rapidly; the peak of emission is only slightly redshifted; and the shift of the bisector with respect to the rest wavelength appears to increase from the center toward the wing, perhaps signifying a gradient in the condensation velocity (Cauzzi et al. 1996). To derive the condensation velocity, we interpret the bisector position at the 30% intensity level in terms of Doppler shifts. While this might underestimate the actual condensation velocity (e.g., Canfield et al. 1990), it is the best compromise between assessing the flows while avoiding contamination from possible blends in the far wings, although these are mostly of photospheric origin. (T. Pereira, private communication) We confirm that similar shifts are derived when using the other triplet lines, albeit with more scatter.

3. PLASMA DYNAMICS

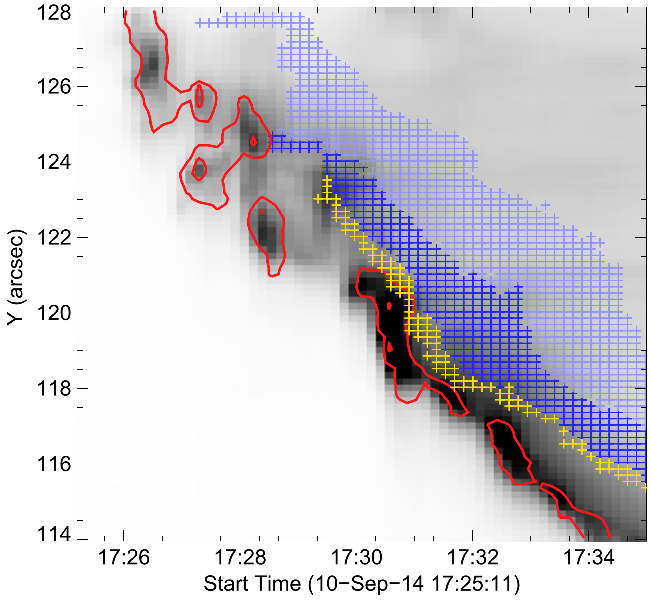

Figure 3. Mg ii intensity spacetime map (inverted B/W color table) with overlays of Mg ii downflows at the 30% bisector level at 15 and 30 km s^{-1} (red contours). The Fe xxi upflow velocities above 270, 200, and 100 km s^{-1} are indicated with yellow, dark blue, and light blue crosses, respectively.

Figure 3 shows a spacetime map for a section of the slit (81 original pixels) where the bright ribbon was found to expand southward at a steady rate of $\sim 0\farcs03$ s^{-1}. These pixels have the cleanest temporal evolution as the ribbon does not dwell over any one of them for longer than one to two time steps. The spatial offset between the Mg ii and Fe xxi detectors was corrected by aligning the spectrograph's fiducial marks.

The Mg ii intensity shows a sudden enhancement due to the flare, and the development of the ribbon clearly appears as a diagonal strip across the diagram. The chromospheric downflows are co-spatial and co-temporal with each of the new intensity enhancements, as shown by the red contours at the 15 and 30 km s^{-1} levels. These values of condensation flows are consistent with results from many earlier ground- and space-based studies, but Figure 3 offers unprecedented detail on their spatial and temporal evolution.

The corresponding evaporation velocities, as derived from the centroid of the Fe xxi fits, are overlaid as colored crosses on the same figure. For about 70% of the pixels, we find flows reaching nearly 300 km s^{-1} (yellow crosses identify flows above 270 km s^{-1}), these encompass the fastest, early Fe xxi emission, pertaining to a very thin spatio-temporal strip approaching our $0\farcs5$ resolution, and lasting only one to two temporal steps. Such values of evaporation flows are among the strongest ever reported (300–400 km s^{-1}; e.g., Antonucci et al. 1982) and the largest documented yet from *IRIS*. Within the same pixels, the flows decay to 200 km s^{-1} (dark blue region) and below rather uniformly in time. For pixels northward of $124''$, we detect only slower flows, up to ~150 km s^{-1}.

From Figure 3, we see that all flaring pixels display clear signatures of both evaporation and condensation, yet the onset of opposite flows is co-temporal (within one to two time steps) for only a few; for most pixels, the initial coronal upflow lags behind the condensation by a minute or more. The delay could be due to a number of reasons: the Fe xxi line could be so blueshifted to fall outside of the detector's edge; the initial emission be too weak to be detected at its earliest inception; or the same pixel Mg ii and Fe xxi signatures could derive from distinct flare loops, depending on their orientation with respect to the line of sight. Yet, this appears unlikely because of the flare's geometry and evolution: *SDO*/AIA 131 Å images

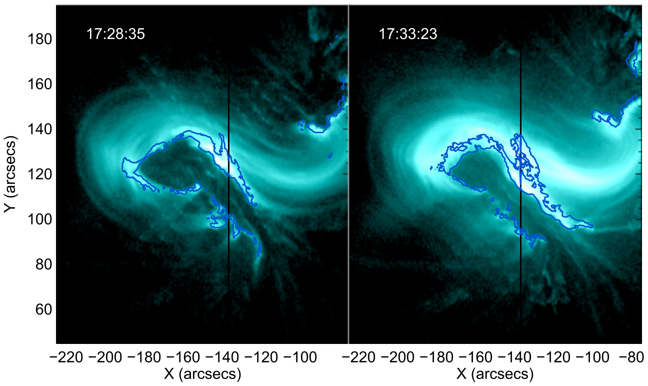

Figure 4. *SDO*/AIA 131 Å images at two times during the impulsive phase, highlighting the geometry of the hot flare loops. The contours show the *IRIS* SJI 1400 Å 800DN level.

(mostly showing Fe xxi emission during flares; Simões et al. 2015) clearly show that the hot flare loops display a dominant E–W orientation, with little line-of-sight superposition of the loops and ribbons (Figure 4).

While plausible that a previously activated hot loop could "cloud" a new ribbon kernel developing southward of it, this should lead to Fe xxi flows appearing at that spatial pixel *before* the chromospheric flows, contrary to what was observed.

We also note that similar delays (~60–75 s) between chromospheric and coronal flows have been reported for other flares (Young et al. 2015; J. Brosius 2015, private communication).

4. TEMPORAL EVOLUTION OF FLOWS

In Figure 5, we show the full evolution of both Fe and Mg velocities for every slit position of Figure 3. To highlight commonalities in the evolution, we perform a superposed epoch analysis by shifting the curves to a common time origin. As the spatio-temporal coincidence of flows between both lines is not certain (Figure 3), we use a different time origin for each: the Fe xxi curves (left panel) are shifted so that the earliest detectable fit occurs at $t = 0$, while in Mg ii (right panel), the velocity curves are aligned to their peak time. For each time step, the number of spatial pixels with velocity between $\delta v = 5$ km s^{-1} (Fe xxi) and $\delta v = 1$ km s^{-1} (Mg ii) is represented by the grayscale, with a maximum (black) of 20 occurrences.

In Fe xxi, all of the pixels experience an instantaneous appearance of the fastest upflows, and although the centroids for the Fe xxi fit are allowed freedom over the entire *IRIS* window ($a \sim 380$ km s^{-1} interval), there is very little random variation in velocity between time steps (the averaged uncertainty drops from ±15 to ±2 km s^{-1} within 50 s). The majority of pixels fall consistently on a very narrow curve, with an initial velocity around 300 km s^{-1} and a decaying upflow lasting over 6 minutes. The smaller grouping of pixels to the north of Figure 3 have instead slower initial flows and plateau earlier, but their decay curve is comparable in shape.

The evolution of evaporation upflows in spatially resolved sources has been discussed only in a handful of papers.[1] In the case of a single flaring footpoint, Brosius (2013), Polito et al. (2015), and Tian et al. (2015) all found velocity curves similar to those displayed in Figure 5, but with decay times ranging between ~3 and 8 minutes, possibly due to differences in the respective data's temporal (9.4–75 s) and spatial sampling. Given the large number of individual flaring kernels represented, the high cadence of the measurements, and the homogeneity of the results, we think that Figure 5 represents the best picture to date of hot evaporating flaring plasma.

In Mg ii, strong condensation downflows are apparent, reaching nearly 40 km s^{-1}. Again, most pixels fall on a very consistent curve, which decays rapidly and approaches near zero velocity in only ~50–60 s. This is in very good agreement with predictions from theoretical models of chromospheric condensation; for example, for typical pre-flare chromospheric conditions, Fisher (1989) indicates 1 minute as the necessary time for the condensation to stop, essentially independent from the flare energy input. Most of the previous condensation studies found a much longer decay time, around 2–3 minutes (Ichimoto & Kurokawa 1984; Ding et al. 1995). It is likely that their results depended on a superposition of unresolved events, occurring successively within their spatial resolution elements (typical pixel size of ~2″–3″).

5. DISCUSSION AND CONCLUSIONS

We have presented a unique *IRIS* data set, covering the development of a large portion of a ribbon during the impulsive phase of an X-class flare. The favorable positioning of the spectrograph slit allowed us to observe several tens of resolved flaring areas, and to follow their complete temporal evolution at high cadence. In this letter we concentrated on their dynamical properties; our main conclusions are as follows.

(1) All of the flaring pixels (at ~0″.5 resolution) display sudden and strong Fe xxi upflows at the beginning of the flare, and we find that the coronal line is *always* entirely blueshifted. This is consistent with other recent *IRIS* results and seems to imply that *IRIS* observations fully resolve single flaring kernels. Still, upflows persist in any given position for a remarkable length of time, and should be readily visible even at the coarser resolution of CDS or EIS (cf. Figure 3), contrary the commonly reported occurrence of a dominant stationary component in such observations. A possible explanation might reside in the very simple linear progression of the newly activated kernels analyzed. However, we cannot state if these observed characteristics are representative of the entire flare or of other events.

(2) All of the flaring pixels (at ~0″.3 resolution) also display sudden and strong Mg ii condensation downflows, with values in agreement with earlier results from both visible and EUV observations. The chromospheric condensation in each flaring kernel stops in ~50–60 s, at least a factor of two faster than any previously reported value, but consistent with predictions of 1D hydrodynamical simulations of flares affecting "undisturbed" chromosphere.

(3) Surprisingly, only a few pixels show a simultaneous onset of coronal and chromospheric flows, while for most of them the initial coronal evaporation lags behind the chromospheric condensation by an average of 68 s. This appears contrary to the standard explosive scenario. From an analysis of the coronal loop geometry, line-of-sight superposition effects do not seem sufficient to explain this delay. As the same trend has been reported in other recent *IRIS* studies, we speculate that the delay could simply be caused by the Fe xxi emission being too weak to be detected at its earliest inception.

---

[1] We note that similar velocity evolution curves have been observed for the case of two X-class flares by Hudson et al. (2011) using disk-integrated EVE data.

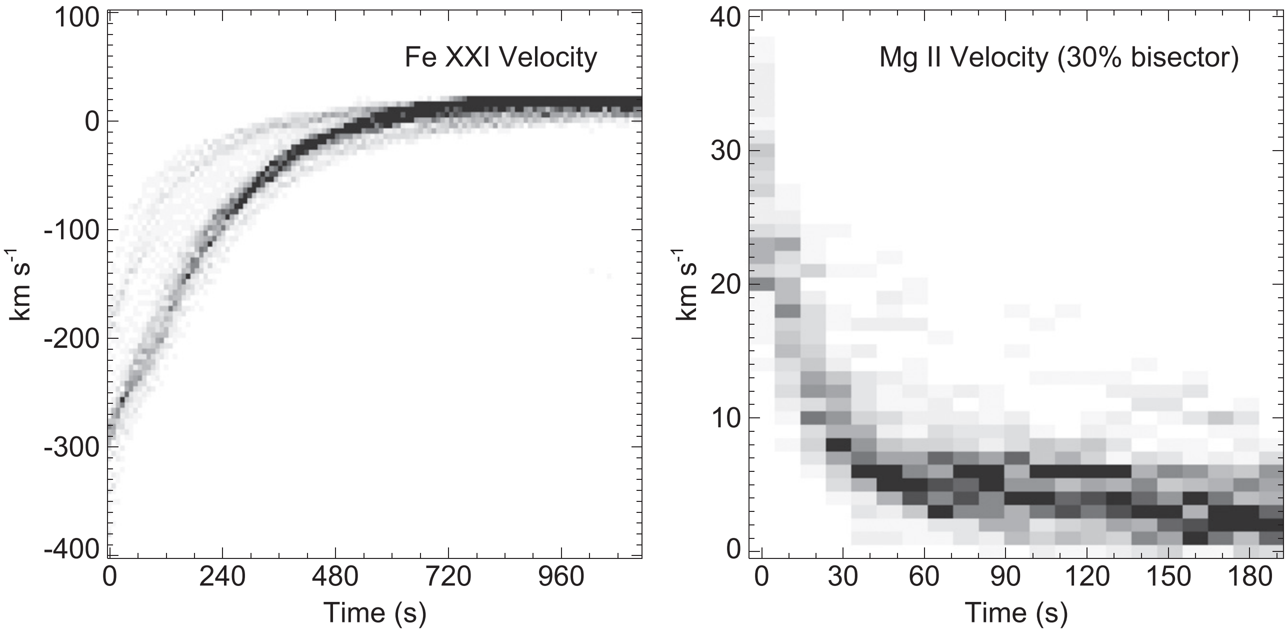

Figure 5. Superposed epoch analysis of Fe XXI and Mg II flows for every slit pixel in Figure 3 (negative velocities showing rising material). The grayscale darkens with increasing occurrence within a given velocity interval (see the text for full detail).

(4) The Fe XXI spectra are extremely broadened compared to the ion's thermal FWHM of 92 km s^{-1} (see Figure 2). Polito et al. (2015) find similar excess broadening and discuss its potential origins, including a plasma temperature beyond the equilibrium formation temperature and unresolved plasma motions, the latter seeming probable when considering the initial rapid change in velocity (Figure 5) for individual pixels.

(5) Figure 5 represents the clearest picture to date of the temporal evolution of both chromospheric evaporation and condensation. The evolution of plasma dynamics is so strikingly similar for most of the pixels it suggests that the characteristics of the energy release are either remarkably uniform, each time occurring in a pristine environment, or have little influence over the subsequent plasma evolution.

We conclude by remarking that the large number of independent flaring pixels observed and the complete temporal coverage of their dynamical evolution at high cadence allow us to derive common characteristics of what we can define as "prototypical" flares, with a spatial extension limited by the actual resolution of our data, i.e., $\leqslant 0''.5$. In principle, our results can be immediately compared with the output of numerical simulations of single flaring loops. For example, with respect to the third point above, one could attempt to derive values of the actual coronal emission during the early phases of flare chromospheric heating, as predicted within either collisional thick-target (Allred et al. 2005) or conductive (Longcope 2014) models.

This research has received funding from the European Community's Seventh Framework Programme (FP7/2007-2013) under grant agreement No. 606862 (F-CHROMA). *IRIS* is a NASA small explorer mission developed and operated by LMSAL with mission operations executed at NASA Ames Research center and major contributions to downlink communications funded by the Norwegian Space Center (NSC, Norway) through an ESA PRODEX contract. We thank L. Fletcher, H. Hudson, R. Falciani, and the two referees for their helpful comments and discussion.

REFERENCES

Allred, J. C., Hawley, S. L., Abbett, W. P., & Carlsson, M. 2005, ApJ, 630, 573
Antonucci, E., Gabriel, A. H., Acton, L. W., et al. 1982, SoPh, 78, 107
Brosius, J. W. 2013, ApJ, 762, 133
Canfield, R. C., Penn, M. J., Wulser, J.-P., & Kiplinger, A. L. 1990, ApJ, 363, 318
Cauzzi, G., Falchi, A., Falciani, R., & Smaldone, L. A. 1996, A&A, 306, 625
Cheng, C.-C. 1990, ApJ, 349, 362
Culhane, J. L., Harra, L. K., James, A. M., et al. 2007, SoPh, 243, 19
De Pontieu, B., Title, A. M., Lemen, J. R., et al. 2014, SoPh, 289, 2733
Ding, M. D., Fang, C., & Huang, Y. R. 1995, SoPh, 158, 81
Doschek, G. A., & Warren, H. P. 2005, ApJ, 629, 1150
Falchi, A., Qiu, J., & Cauzzi, G. 1997, A&A, 328, 371
Fisher, G. H. 1987, ApJ, 317, 502
Fisher, G. H. 1989, ApJ, 346, 1019
Graham, D. R., Fletcher, L., & Hannah, I. G. 2011, A&A, 532, A27
Harrison, R. A., Sawyer, E. C., Carter, M. K., et al. 1995, SoPh, 162, 233
Hori, K., Yokoyama, T., Kosugi, T., & Shibata, K. 1997, ApJ, 489, 426
Hudson, H. S., Woods, T. N., Chamberlin, P. C., et al. 2011, SoPh, 273, 69
Ichimoto, K., & Kurokawa, H. 1984, SoPh, 93, 105
Leenaarts, J., Pereira, T. M. D., Carlsson, M., Uitenbroek, H., & De Pontieu, B. 2013, ApJ, 772, 90
Li, P., Emslie, A. G., & Mariska, J. T. 1989, ApJ, 341, 1075
Li, T., & Zhang, J. 2015, ApJL, 804, L8
Longcope, D. W. 2014, ApJ, 795, 10
Mariska, J. T., Emslie, A. G., & Li, P. 1989, ApJ, 341, 1067
Mason, H. E., Shine, R. A., Gurman, J. B., & Harrison, R. A. 1986, ApJ, 309, 435
Meegan, C., Lichti, G., Bhat, P. N., et al. 2009, ApJ, 702, 791
Milligan, R. O. 2015, arXiv:1501.04829v2
Milligan, R. O., & Dennis, B. R. 2009, ApJ, 699, 968
Milligan, R. O., Gallagher, P. T., Mathioudakis, M., et al. 2006, ApJL, 638, L117
Pereira, T. M. D., Carlsson, M., De Pontieu, B., & Hansteen, V. 2015, ApJ, 806, 14
Polito, V., Reeves, K. K., Del Zanna, G., Golub, L., & Mason, H. E. 2015, ApJ, 803, 84
Sadykov, V. M., Vargas Dominguez, S., Kosovichev, A. G., et al. 2014, ApJ, 805, 167
Simões, P. J. A., Graham, D. R., & Fletcher, L. 2015, SoPh, in press
Tian, H., Li, G., Reeves, K. K., et al. 2014, ApJL, 797, L14
Tian, H., Young, P. R., Reeves, K. K., et al. 2015, arXiv:1505.02736
Young, P. R., Tian, H., & Jaeggli, S. 2015, ApJ, 799, 218